PHYSICAL REVIEW ACCELERATORS AND BEAMS **26,** 020101 (2023)

Toward transparent injection with a multipole injection kicker in a storage ring

R. Ollier, P. Alexandre, R. Ben El Fekih, A. Gamelin, N. Hubert, M. Labat,
L. S. Nadolski, and M.-A. Tordeux[*]
Synchrotron SOLEIL, L'Orme des Merisiers, Saint-Aubin, France

(Received 27 June 2022; accepted 3 January 2023; published 21 February 2023)

Achieving transparent Top-Up injection, characterized by stored beam position perturbations lower than 10% of the root mean square (rms) size of the stored beam, is very challenging for third-generation storage ring-based synchrotron light sources. The standard bump-based injection scheme used at SOLEIL 2.75-GeV storage ring for daily operation relies on two pulsed septum magnets and four pulsed dipole kickers installed in a 12-m-long straight section. Perfect tuning of the kickers to meet the perturbation tolerances is impossible since it would require at least four identical magnets, Ti-coated ceramic chambers, and electronics. On the way toward transparent injection, the four kickers can be replaced by a single pulsed magnet, benefiting from a field-free region in the stored beam path. This Multipole Injection Kicker (MIK), developed in the frame of a collaboration between SOLEIL and MAX IV, and currently installed in the MAX IV 3-GeV storage ring, has proven to meet the transparency specifications. A copy of the MIK has been installed in a short straight section of the SOLEIL storage ring in January 2021. Perturbations of less than 2% of the rms size of the stored beam were measured using the newly installed high-performance diagnostics. In this article, a start-to-end model of the MIK-based injection is presented as well as major challenges inherent in designing such an innovative magnet. Then, the results of the MIK commissioning are presented in depth along with the high-performance diagnostics, which are essential when such levels of beam stability are to be achieved.

DOI: 10.1103/PhysRevAccelBeams.26.020101

I. INTRODUCTION

Synchrotron light sources are user facilities that simultaneously deliver extremely intense photon beams to dozens of 24/7 experimental stations, called beamlines, located around the circumference of their storage ring. High brightness, flux, and coherence of the photons are achieved thanks to a highly focused ultrarelativistic electron beam passing through magnetic structures such as dipoles or insertion devices. The electrons are distributed longitudinally in bunches created by a radio-frequency (rf) system compensating on average for the radiation energy loss over each revolution turn. In the case of third-generation light sources, the emittance is in the range of a few nanometers-radians for typically 2 to 8-GeV storage rings. The stability in position, angle, and size of the photon beam is directly related to that of the electron beam: in the past, the required position stability was 10% of the root mean square (rms) beam sizes; today, the stability criteria are even more stringent and can reach 2 to 3% for some beamlines. This translates into submicrometer stability that can only be reached if the thermal load, mainly due to the photon beam (energy deposited on the mirrors and absorbers) and the stored electron beam (impedance effect and collective effects), is maintained at all times on both the optical components of the beamlines and on the accelerator equipment. The only way to achieve this goal is by continuous injection, or Top-Up injection mode, where, on average, every few minutes or less, new electrons are injected at each fixed time interval or as soon as the average electron beam current drops by typically a fraction of 1% of the total current. Since designing an injection system that does not disturb the stored beam is practically impossible, the beamlines often record altered signals when injection occurs. This is particularly the case for infrared or nanobeam beamlines and beamlines working on a time scale comparable to the injection event. Moreover, it is not always possible to filter the noise introduced by the injection events from the recorded signals.

Most injection schemes of third-generation synchrotron light sources are based on off-axis injection geometry, implementing in and out of vacuum pulsed dipole magnets preferably in a single straight section if the space needed is available. A local orbit bump of the stored beam is created

---

[*] Corresponding author.
laurent.nadolski@synchrotron-soleil.fr

to facilitate the capture of the injected beam. The pulse duration of the fast dipolar magnets lasts for one or a few revolution periods depending on the limits of the technology and the injection requirements. Residual dipolar kicks due to the unavoidable nonclosure of the bump (because of discrepancies between the magnets, slight differences in the titanium coated ceramic chambers, and the performance of the electronics...) result in betatron oscillations. Besides, the bump-based injection scheme suffers additional perturbations, regardless of kicker pulse matching optimizations, when nonlinear magnets are interposed between the pulsed kicker magnets for the reason of available space in the storage ring, as indicated by several simulation and experimental studies [1–3]. Emittance beating could also be generated along the injection process if the beam experiences quadrupolar kicks or coupling due to higher order nonlinear magnets included in the bump. To overcome these limitations, the development of non-linear kicker (NLK) magnets has become a major R&D subject at storage ring-based synchrotron light sources since the first successful use of a pulsed sextupole magnet as a key element of an injection scheme, at KEK-PF, in 2010 [4]. Nevertheless, the technology required to make an NLK is very challenging and many difficulties need to be overcome to reach the expected performance and high reliability in operation.

In the frame of the collaboration between Sweden and France between 2012 and 2017, SOLEIL has designed and built a Multipole Injection Kicker (MIK) for the 3-GeV ring of MAX IV light source, starting from the design of an NLK developed by BESSY and further MAX IV design work [3,5,6]. The first MIK device was installed in 2017 prior to an improved version in 2019 with a thicker Ti coating that reduced heating induced by the circulating beam. The amplitude of the residual betatron oscillations due to the MIK, scaled to the center of the long straight section, was reduced below 7 μm rms in both planes as reported in [7,8]. In the wake of this success, SOLEIL decided to build its own copy of the MIK as a possible alternative to the present injection system and as an R&D device to gather more experience from the perspective of fourth-generation ring-based light sources. The MIK was installed into the 2.75-GeV storage ring of SOLEIL and its commissioning started in January 2021 [9].

This article starts with a description of the standard injection scheme of SOLEIL in the next section. Its performance in terms of injection efficiency and impact on the stored beam stability are reported. Then, the principle and specifications of the innovative MIK-based injection scheme are described. In Sec. III, we introduce the mechanical and magnetic design as well as assembly of the MIK. Then, the simulation studies that led to the location of the MIK, the optimal injection parameters, and the expected performance are discussed in Sec. IV. In the following section, we provide an overview of the newly commissioned set of diagnostics used to characterize the MIK injection turn-by-turn. This leads to the presentation of the main experimental results in Sec. VI. To conclude, the main achievements are recalled in Sec. VII, which paves the way to future experiments related to the current operation of the beamlines and the SOLEIL Upgrade project [10–12].

In the remainder of this article, a point in space is defined by the triplet (x, z, s), each coordinate, respectively, representing the horizontal, vertical, and longitudinal position with respect to the ideal particle.

II. INJECTION SCHEMES FOR TOP-UP OPERATION AT SOLEIL

A. SOLEIL accelerator complex

The SOLEIL accelerator complex consists of a 110-MeV linear accelerator and a full-energy booster injector (Table I) injecting into a 354-m circumference storage ring [13,14]. Photon beams have been delivered 5000 h a year to 29 beamlines since January 2008. The storage ring lattice consists of 16 double-bend achromat cells, implementing a modified Chasman-Green lattice, i.e., the horizontal dispersion is nonzero in the straight sections of the storage ring in order to decrease the horizontal emittance to 3.9 nm rad. For half of the cells, the achromat was split into two in order to create eight additional 3.6-m-long short straight sections [15]. This compact light source exhibits 24 straight sections. Figure 1 gives the linear optics of a quarter of the storage ring and the major characteristics are recalled in Table II.

The dynamic aperture given at the injection point, which is located in the middle of the injection section of the storage ring, ranges between −13 and 11 mm horizontally and ±4 mm vertically (Fig. 2). The betatron amplitude of the injected beam equals roughly −9 mm. The injection section hosts all the necessary pulsed magnets for Top-Up operation. The nominal injection layout is depicted in Fig. 3 and detailed in the following.

B. Current off-axis injection layout

The current injection scheme used at SOLEIL for Top-Up operation relies partly on the thick and thin septum magnets, together with four dipole kicker magnets installed in a long straight section of 12 m [17] (see Fig. 3). When injecting, a

TABLE I. Main parameters of the SOLEIL injector.

Parameter	Value
Circumference (m)	156.6
Revolution period (ns)	522
Harmonic number	184
Natural emittance (nm rad)	135
Natural energy spread	6.67×10^{-4}
Bunch length (mm)	29

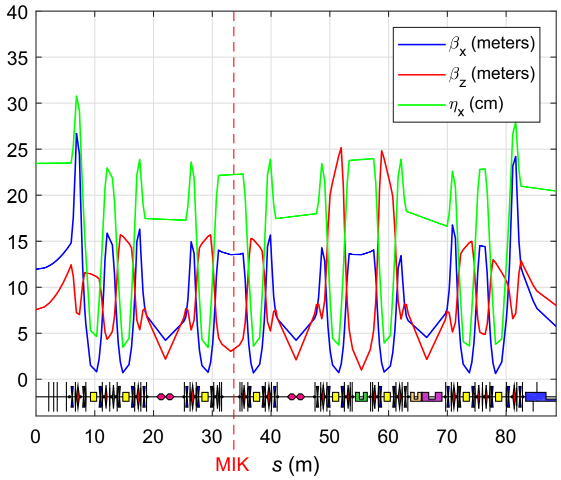

FIG. 1. Twiss functions of a quarter of the SOLEIL storage ring. Horizontal and vertical betatron functions (β_x, β_z) are plotted in blue and red solid lines, respectively, while the horizontal dispersion η_x corresponds to the green solid line. The electromagnetic elements of the lattice are drawn at the bottom of the figure: dipoles (yellow), focusing and defocusing quadrupoles (blue and red), sextupoles (pink and green), and rf cavities are in the first to medium straight sections around $s = 20$ and 40 m (pink) while remaining short and medium straight sections are filled with insertion devices. The black dots and vertical bars symbolize BPMs and correctors, respectively.

pulsed horizontal bump is induced by the four kickers to bring the stored beam as close as possible to the injected beam path, while, in the meantime, the on-momentum injected beam is brought parallel to the stored beam thanks to the consecutive kicks of the septum magnets. Both beams must propagate as close as possible to the thin septum blade, in order to minimize the required horizontal dynamic aperture. The half horizontal dynamic aperture is on the order of 13 mm at SOLEIL. The minimum half horizontal dynamic aperture needed in operation is approximately 13 mm as well (knowing that the septum blade is 3.5 mm thick and assuming that the rms injected and stored beam sizes are 1.2 mm and 320 μm, respectively, and their clearance equal to 3 and 7, respectively). This minimum horizontal dynamic aperture can be optimized by means of an emittance exchange in the booster, as presented in [18], to enhance injection efficiency.

TABLE II. Main parameters of the SOLEIL storage ring.

Parameter	Value
Energy (GeV)	2.75
Circumference/revolution period (m/μs)	354.1/1.18
Natural emittance (nm rad)	3.9
Energy spread	1.016×10^{-3}
Horizontal/vertical betatron tunes (ν_x, ν_z)	(18.156, 10.228)
Horizontal/vertical corrected chromaticities (ξ_x, ξ_z)	(1.2, 2.4)
Bunch length (mm)	4.6
Horizontal/vertical/longitudinal radiation damping time (ms)	6.9/6.9/3.16
Betatron functions[a] (β_x, β_z) (m)	12.1/7.8
Horizontal/vertical stored beam sizes[a] (μm)	320/22
Horizontal/vertical injection beam sizes[a] (mm)	1.2/0.6
Betatron functions (β_x, β_z) at MIK (m)	13.5/3.2
Harmonic number	416
rf frequency/voltage (MHz/MV)	352.2/2.8

[a] Computed at the injection point.

Eventually, the stored beam is brought back to its original closed orbit, along with the injected beam, as the orbit bump falls. The beam coming from the injector is injected off-axis and enclosed in the dynamic aperture (see Fig. 2). Consequently, the injected beam starts to perform horizontal betatron oscillations around the closed orbit with a dozen millimeters amplitude. Eventually, the injected beam merges with the stored beam after a few radiation damping times. In the bare lattice, the injection efficiency was measured to be around 95%. However, a major modification of the lattice occurred in the summer of 2021: one of the standard 1.71 T dipole was replaced by a permanent magnet–based 2.8-T superbend [14]. Although the settings of the quadrupoles and the sextupoles were adjusted to restore the tunes and chromaticities to their values preceding the commissioning of the superbend, the dynamic aperture was significantly reduced due to the strong sextupolar component of the superbend. Thus, the injection efficiency dropped by 15%.

Preserving the stability of the stored beam is at least as important as maximizing the injection efficiency. Extensive work has been performed over the years to reduce the

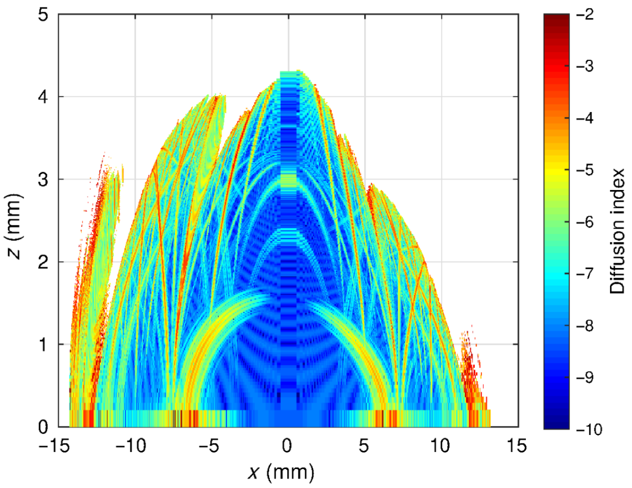

FIG. 2. Dynamic aperture of the bare lattice, including the permanent magnet–based 2.8 T superbend magnet (presented in Sec. II B). All the scrapers are fully extracted and the septum blade is inserted to −19.5 mm. The color code refers to the diffusion index of the tune for 1000 turns using frequency map analysis [16].

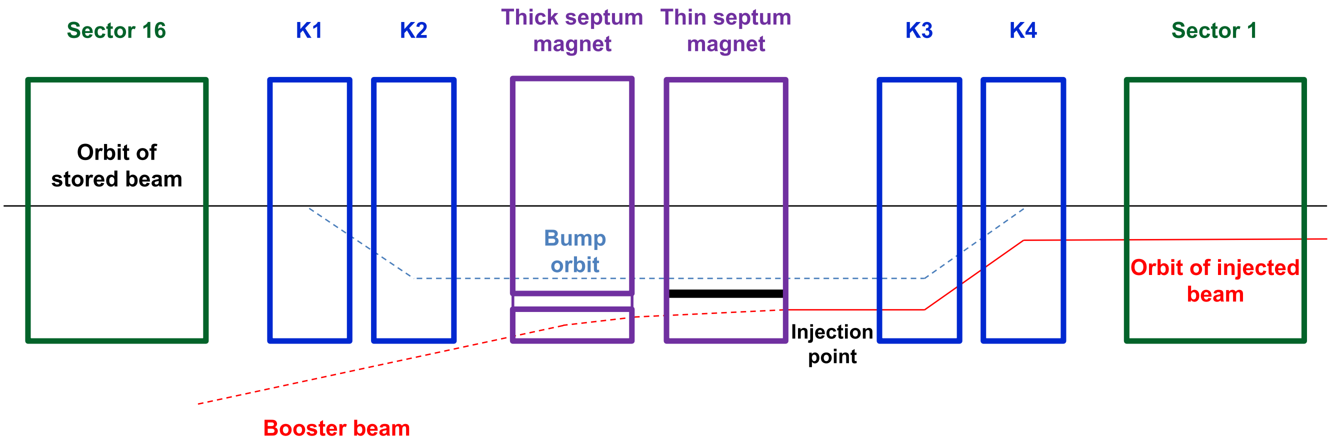

FIG. 3. Standard bump-based injection scheme. The stored beam is bumped (blue dashed line) from the central orbit (black solid line) by the four kickers (blue squares), in the injection section. The booster beam (red dotted line) is brought parallel to the stored beam by the septum magnets (in purple). Eventually, the stored beam is brought back to the central orbit with the injected beam (red solid line), as the orbit bump falls.

detrimental side effects of the injection magnets on the closed orbit. Indeed, delicate shielding was added around the chamber of the septum magnets, the excitation wave was changed from half to full sine for the thin septum, the Eddy current was grounded for the thick septum, and the pulse profile as well as roll angle of each kicker magnet were finely tuned over the entire 7 μs pulse (Table III). Despite all these efforts, the kickers still accounted for the major part of the peak stored beam position perturbations, minimized to 31% and 250% of the rms stored beam size in the horizontal and vertical planes, respectively [19–22] (see summary in Table IV). Therefore, replacing the four kickers by a single MIK with its field-free region at the location of the stored beam path appears as a great asset to drastically reduce the disturbances.

C. MIK off-axis injection layout

In order to achieve transparent Top-Up injection, the four kickers are replaced by a single MIK (see Fig. 4). It is located roughly 32 m downstream of the injection point with a horizontal phase advance of 10.42 rad. The MIK is made to leave the closed orbit unperturbed, as the stored beam propagates through the field-free region. In this off-axis injection scheme, the injected beam is still brought as close as possible to the outer face of the septum blade. The thin septum was motorized in order to insert the inner face of its blade at −17.5 mm from the longitudinal axis of the ring, i.e., 2 mm further than in standard operation. The injection point is set up so that the injected beam can freely oscillate with amplitudes on the order of 25 mm and reach the peak magnetic field of the MIK at a target position $(x, z) = (10.3\ \mathrm{mm}, 0\ \mathrm{mm})$. During its first pass, the injected beam interacts with the nominal magnetic field of the MIK, which minimizes the oscillation amplitudes to approximately 10 mm. This is the reduction principle of the injection invariant, as presented in [4]. Thus, the injected beam oscillates within the dynamic aperture. Because of its large transverse size, the injected beam is not uniformly kicked by the MIK and exhibits the footprint of a multipolar magnetic field, as illustrated in Fig. 5.

Ultimately, the objectives of the standard and MIK injection schemes are effectively the same. However, the MIK is a technological innovation because of its design, the way it is engineered and integrated into the storage ring, and its performance. As mentioned, one of the crucial points for achieving reliable transparent injections is the multipole magnetic field, which is highly dependent on the mechanical design of the MIK.

TABLE III. Main design parameters of the standard injection pulsed magnets.

Parameter	Kickers	Thick septum	Thin septum
Wave form	Half sine	Half sine	Full sine
Magnetic length (m)	0.60	2×0.50	0.60
Pulse duration (μs)	7	3.3×10^3	120
Nominal kick (mrad)	±5.8	110	25

TABLE IV. Optimized characteristics and perturbations of the injection devices.

Parameter	Thick/Thin septum	Kickers
Pulse duration (μs)	$3.3 \times 10^3/120$	7
Deflection angle (mrad)	110/25	±5.8
Maximum horizontal oscillation amplitude (μm)	6/0% of σ_x	31% of σ_x
Maximum vertical oscillation amplitude (μm)	25/0% of σ_z	250% of σ_z

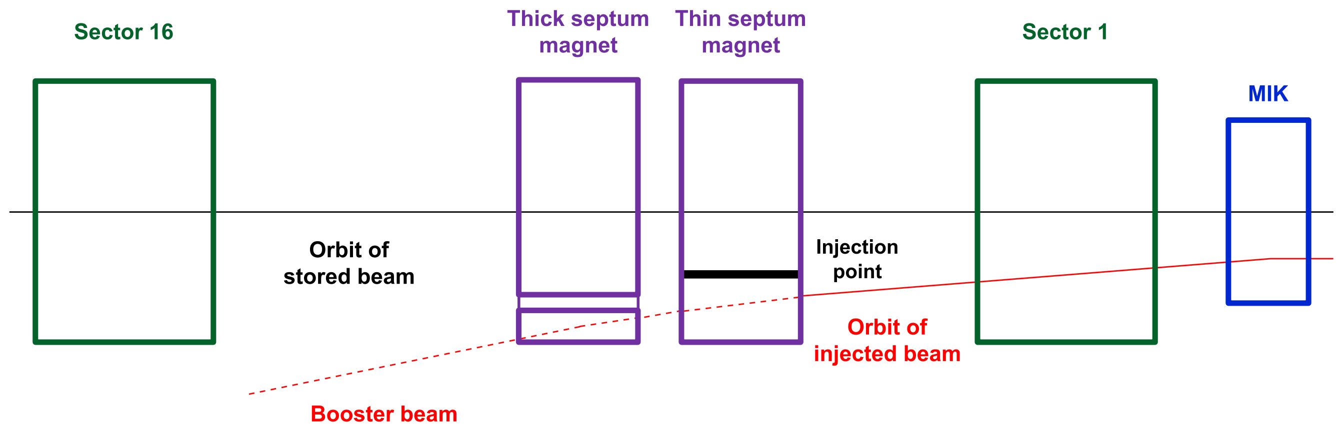

FIG. 4. MIK injection scheme. The orbit of the stored beam is left unperturbed (black solid line), while the booster beam (red dotted line) is brought close to the septum blade thanks to the septum magnets (in purple). The injected beam propagates freely (red solid line) until the amplitude of the horizontal oscillation is minimized by the MIK (blue square).

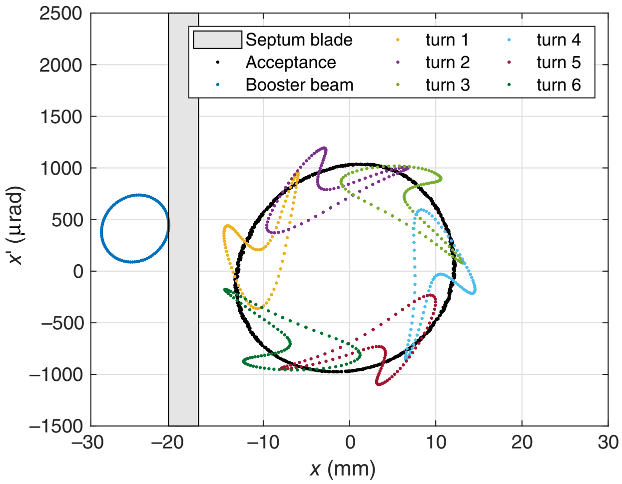

FIG. 5. Simulated MIK injection: at the injection point, the booster beam (100 blue dots 3σ envelope) is injected close to the septum blade (shaded area) outer face and captured within the dynamic aperture (black dots) after the MIK kick. Because of its size, the injected beam (multicolor) exhibits the footprint of the MIK field during the first turns (six represented).

III. MIK DESIGN

A. Mechanical design and assembly

The MIK installed at SOLEIL is identical to that of MAX IV as both were designed during the 2012–2017 collaboration between the two laboratories [3,6,8]. The main design parameters of the MIK are given in Table V.

Its vacuum chamber is made out of a bulk of sapphire manufactured by Kyocera™. Eight grooves are precisely machined longitudinally and house the conductors that form the electromagnet (see Fig. 6). Careful assembly of the eight conductors with radiation resistant epoxy glue was performed at SOLEIL, after the chamber had been coated with a thin layer of sputtered titanium at the European Synchrotron Radiation Facility (ESRF) [23]. The thickness of the coating, equal to 3.5 μm, is estimated to balance the heat load deposited by the beam-induced image currents and the attenuation of the pulsed magnetic field due to the pulse-induced Eddy currents.

The main engineering work in order to install the MIK in the SOLEIL storage ring was to adapt its physical aperture to that of the surrounding chambers. Following the electron beam, a standard taper-absorber reduces the aperture from ±35 mm (horizontal) and ±12.5 mm (vertical) to ±23 mm (horizontal) and ±5.8 mm (vertical). It intercepts most of the synchrotron radiation generated from the upstream bending magnet and provides pumping capability with an attached ion pump. A secondary newly designed taper-absorber was also required to match the aperture of the MIK. With 46.8 mm (horizontal) and 7.8 mm (vertical.), it is the smallest fixed physical aperture of the storage ring. The tip of this taper is inserted to 20.4 and −23 mm in order to fully protect the MIK from synchrotron radiation, including the possibility of electron or photon beam misalignment. This secondary taper-absorber including

TABLE V. Main design specifications of the MIK.

Parameter	Value
Horizontal/vertical physical aperture (mm)	46.8/7.8
Total mechanical length (flange-to-flange) (mm)	400
Magnetic length (mm)	304
Magnetic field at target position (mT/kA)	24.85
Horizontal/vertical field-free region (μm)	800/100
Pulse duration (μs)	2.4
Target horizontal/vertical position at MIK (mm)	10.3/0.0
Nominal voltage (kV)	10
Nominal peak current (kA)	3.3
Nominal horizontal kick θ_x (mrad)	2.2

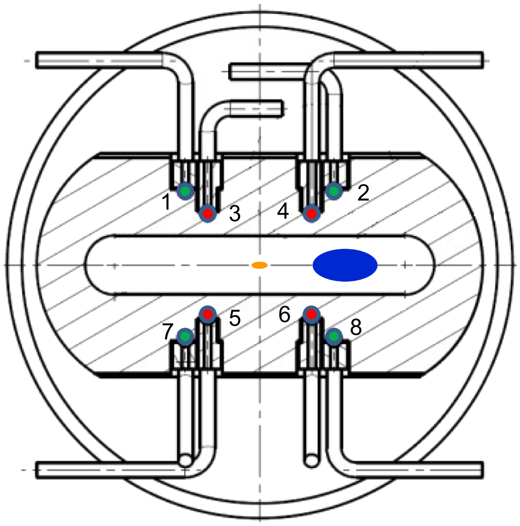

FIG. 6. Front view of the MIK cross section with red and green copper rods numbered from 1 to 8, striped sapphire vacuum chamber (46.8 mm (H) ×7.8 mm (V) physical aperture), injected (blue), and stored (orange) beams. The red and green dots on the conductors represent the current direction.

the two ConFlat™ flanges, water circulation circuits, and aperture with tapered shape was entirely machined from a bulk of copper chrome zirconium alloy. The advantage of this manufacturing method is that neither welding nor brazing of vacuum tight parts is required, which is time and cost saving. It also reduces the risk of having rejected parts due to potentially polluted and leaking weld or brazing. A similar combination of secondary and standard taper-absorber is installed at the exit of the MIK (see Fig. 7). So far, the secondary taper-absorber sets, as well as the standard ones, have performed very satisfactorily and the engineering and ultrahigh vacuum groups of SOLEIL are considering more of these machined-in-one parts for the storage ring upgrade.

The main design specifications of the MIK being defined, it is of the utmost importance to meet these specifications in order to generate the ideal magnetic field presented in the next section. Otherwise, even small errors can have negative, although manageable, consequences on the performance of the MIK and the storage ring, as further detailed in the following.

B. Magnetic field topology

The pulsed magnetic field of the MIK is induced thanks to a capacitive resonant discharge pulser, providing half-sine current pulses up to 3.6 kA, under 11 kV. The pulse duration is reduced to 2.4 μs, corresponding to twice the revolution period of the storage ring, in order to avoid strong residual fields which would perturb the injected beam on the turns following the injection.

Since the magnetic length of the MIK equals 304 mm, the longitudinal component of the magnetic field is not taken into account. In the case of an ideal field, the intensity of the longitudinal component, integrated over the conductor length, is typically on the order of -6.0×10^{-4} Tm, at pulse plateau ($t = 1.2$ μs). The momentum vector of the injected beam is almost collinear with $\mathbf{B}_s$ since the horizontal deviation $x'_{\mathrm{MIK}} = -2.2$ mrad and the vertical deviation z'_{MIK} is supposed to be zero. Therefore, the injected beam, and *a fortiori* the stored beam, whose deviations are much lower than that of the injected beam, will not experience significant additional kicks along the MIK because of the deviation induced by B_s. Hence, the magnetic field of the MIK is reduced to the integrated transverse components $B_x(x,z)$ and $B_z(x,z)$. In the thin lens approximation, these field components correspond, respectively, to a vertical kick θ_z and a horizontal kick θ_x. In order to perform transparent Top-Up injection, the MIK has been designed to provide two specific field regions. First, a field-free region in the stored beam path is characterized by $\theta = \sqrt{\theta_x^2 + \theta_z^2} = 0$, at the magnetic center

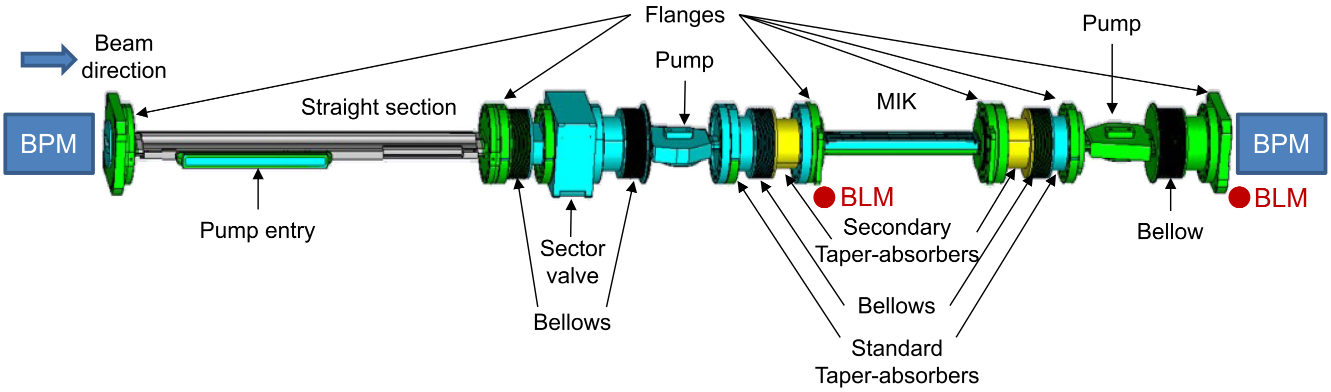

FIG. 7. MIK section. The MIK is installed in a short straight section of the storage ring, which starts and ends with a beam position monitor (blue squares). A pair of taper/absorber chambers, upstream and downstream of the MIK, adapt the physical apertures of the standard vacuum chamber and protect the MIK from the synchrotron radiation. Two beam loss monitors (red dots) surround the MIK for radiation safety purposes. The ultrahigh vacuum is guaranteed by a triplet of pumps.

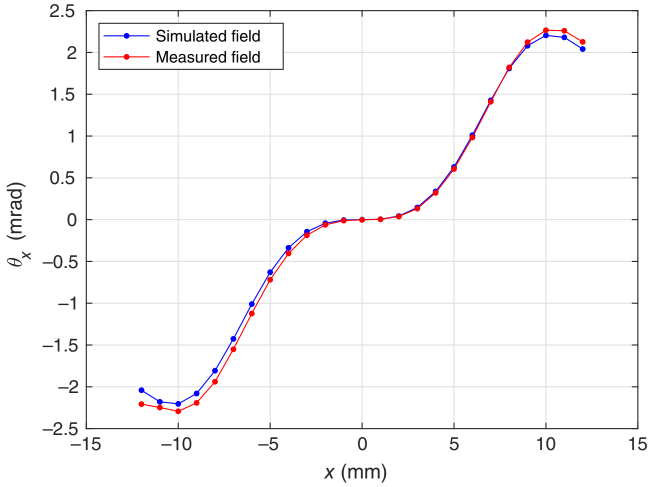

FIG. 8. Horizontal variations of the measured (red) and the ideal simulated (blue) horizontal kick θ_x, at $z = 0$ and $t = 1.2$ μs, scaled to match the operation at 10 kV. The measured field satisfactorily matches the simulated field in the field-free region and on the injected beam path at $x = 10.3$ mm.

of the MIK, and $\theta \leq 1$ μrad for $r = \sqrt{x^2 + z^2} \leq 500$ μm. Second, a nominal field region, at the target position, is characterized by $\theta_x = 2.2$ mrad and $\theta_z = 0$ under 10 kV (see Fig. 8).

At $z = 0$ mm, the vertical field has an octupolar shape, while the horizontal field is zero. However, due to the pulse-induced Eddy currents that propagate in the coating layer, an unwanted weak transient quadrupolar field is induced at the beginning and at the end of the pulse, in the field-free region, as illustrated in Fig. 9. The variations of the octupolar and quadrupolar components of the ideal B_z field, with respect to time, are plotted in [24].

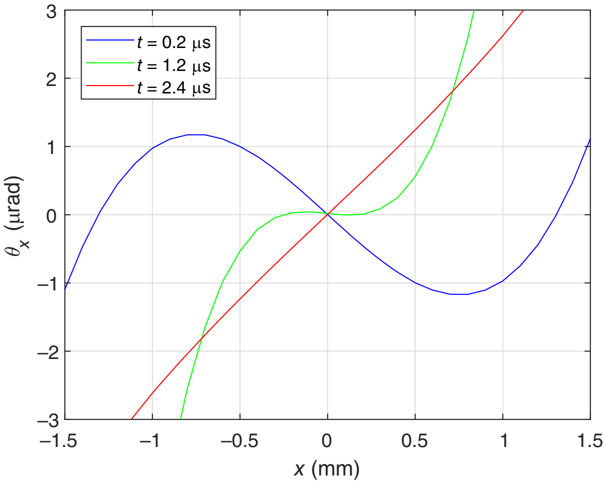

FIG. 9. Variations of θ_x with respect to the horizontal position, under 10 kV at three different times of the pulse. The extrema of the quadrupolar strength are reached during the current rise, at $t = 0.2$ μs (blue), and the current fall, at $t = 2.4$ μs (red), while the field exhibits its nominal octupolar shape at peak current, $t = 1.2$ μs (green).

The transient nonuniform ideal field has been simulated with Quickfield™ Professional [25] as the reference field to perform tracking studies and measurements characterizations. Indeed, the real field of the MIK has been measured at 1 kA, prior to its installation. The vacuum chamber was scanned with an integral pickup coil along the x and z axes and the signal integrated with a high precision oscilloscope. Precision steppers and careful alignment of the test bench and the probe ensure the accuracy of the measurements. The comparison between the measured and simulated fields, converted into kick maps, demonstrates that θ_x meets the specifications (Fig. 8). On the other hand, the measurements of the B_x field exhibit discrepancies with the ideal horizontal field. These discrepancies are due to systematic errors, as they are very reproducible. They result in a residual dipolar error of 15 μT m/kA at the center of the MIK vacuum chamber. After this primary set of measurements, it was not possible to tell if the offset was due to minor defects in the MIK or a misalignment of the magnetic probe. In the end, the beam-based measurements settled the question as explained in the experimental section. Nevertheless, the agreement between the simulated and measured field was consistent enough to pursue the simulation studies with the ideal field.

IV. SIMULATIONS

Several feasibility studies have been conducted prior to the installation and the commissioning of the MIK, using the Accelerator Toolbox (AT) [26], Simulated Commissioning [27], and the TRACY-III code [28]. In each case, the electromagnets of the modeled storage ring are perfectly aligned. All of them are thick elements of the bare lattice, except the correctors. In addition, each magnet is described with its set of measured multipolar fields.

First, the AT model was used to determine the best available location to install the MIK in the storage ring. The phase advance at the MIK location has to ensure a reduction of the Courant-Snyder invariant such that the amplitude of the horizontal betatron oscillations is on the order of 10 mm (see Sec. II C). The simulations predicted the only available section that the injected beam can reach without being lost and which meets the amplitude requirement is the first short straight section of the storage ring from the injection point, at 32 m downstream. The optics of this section is displayed in Fig. 1.

Once the MIK location was validated, the physical apertures of the AT lattice were updated to model the MIK section. The same work has been done with TRACY-III. In the TRACY-III model, the MIK is never switched on as only the impact of the reduction of the vacuum chamber at the MIK section is studied in terms of beam lifetime. The beam lifetime simulations have been carried out to ensure that the MIK section does not affect the performance of the daily operation. The results obtained from the TRACY-III computations were confirmed with beam-based experiments, in the bare lattice first, using the scrapers, and with a typical configuration of the insertion devices: the Touschek lifetime is reduced by 20% when the insertion devices are fully open and below 3 to 5% when they are closed to minimum gaps. It should be noted that these studies did not include the superbend since it was installed afterward.

Conversely, the MIK is switched on and off on purpose in the AT model reproducing its time profile for start-to-end injection simulation. The MIK injection has been optimized thanks to simulated beam loss maps studies carried out with AT. To do so, a six-dimensional Gaussian bunch of 10^4 electrons is injected and tracked over 10^4 turns. The MIK is switched on during the first two turns in the storage ring. During the first turn, the nominal integrated field map of the MIK, corresponding to $t = 1.2$ μs, is interpolated with respect to the positions of the electrons at the MIK location. On the second turn, the same process is repeated for $t = 2.4$ μs so that the tracking includes the effects of the weak residual fields on the transverse dynamics of the injected beam. The simulations showed that the septum blade had to be inserted 2 mm further from its nominal position of -19.5 mm in order to minimize the injection losses. However, the blade must not be inserted any further to prevent the decrease of the Touschek beam lifetime. Consequently, the booster beam is injected horizontally at $x_{\mathrm{inj}} = -26.8$ mm, with an initial slope of $x'_{\mathrm{inj}} = 534$ μrad. The injected beam propagates out of the dynamic aperture until the MIK gives it a horizontal feed-down kick of 2.2 mrad peak, which minimizes the injection invariant from 55 to 7 mm mrad. This is illustrated in Fig. 10, along with two unwanted cases: injection failure (MIK OFF) and MIK strength badly set. In both latter cases, the injected beam performs large betatron oscillations and is even lost during the first turn if the MIK is turned off. Excluding the superbend, the parametric studies showed that the injection loss rate can be as low as 1% if the booster beam coupling is lower than or equal to 20%. It increases by a factor of 10 when the superbend is included in the lattice. In both cases, the electrons are mostly lost on the vertical physical aperture of the medium straight sections of ±5 mm.

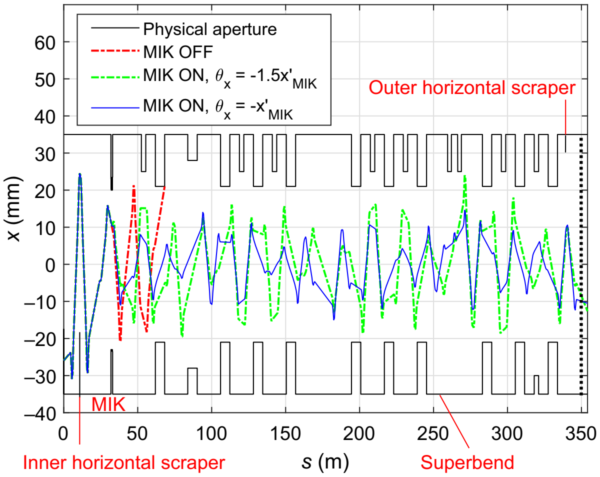

FIG. 10. Horizontal betatron oscillations of the injected beam. If the MIK is switched off, the beam is lost 70 m downstream of the injection point (red dashed curve). If the MIK is switched on, but is too strong (+50% here), then the injected beam oscillates with large amplitude (green dashed curve) and will be lost after a few turns. If the MIK is switched on, and its kick set up to cancel the horizontal deviation of the injected beam at the MIK location, denoted x'_{MIK}, then the oscillation amplitude of the injected beam is minimized passing from roughly 25 to 10 mm after the MIK (blue curve). The horizontal scrapers are inserted to their nominal position and the position of the vertical scrapers is represented by the black dotted line.

The physical aperture of the MIK being the narrowest of the bare machine, a non-negligible part of the decay losses is distributed along the MIK section. The simulations proved in agreement with measurements that these losses can be relocated in the overshielded injection section by inserting the vertical and horizontal scrapers to 3 and 33 mm and -20 mm, respectively. The positions of the scrapers are illustrated in Fig. 10.

The simulations enabled to demonstrate the feasibility of the MIK injection scheme. The parametric studies have led to the definition of an ideal injection preset that allowed to inject and store electrons during the commissioning. All along this process, the simulated data were correlated to the measurements in order to confirm the expectations or adjust some parameters to the needs of the accelerator operation. These measurements were performed thanks to the diagnostics presented in the next section.

V. EXPERIMENTAL SETUP

Knowing that the final goal of the MIK injection is to provide unperturbed stored beam, it was necessary to use high-performance diagnostics to measure accurately the turn-by-turn transverse positions and sizes of the stored beam. In this scope, Libera Brilliance Plus beam position monitor (BPM) electronics as well as an ultrafast KALYPSO camera have been used for the measurements [29,30]. They provided unprecedented performance at SOLEIL which enabled to reach the ultimate levels of perturbations measurable regarding the experimental conditions. The injection losses were also followed on a turn-by-turn basis using beam loss monitors (BLMs). Beam loss monitoring is indeed of great interest since the devices may suffer damages, especially the MIK which is a brittle magnet, or maybe overactivated, preventing any human intervention on them in a reasonable time. Those three diagnostics were specifically commissioned for the MIK experiments.

A. Newly commissioned turn-by-turn diagnostics

1. Beam position monitors

The 122 Beam Position Monitors (BPMs) installed in the storage ring are composed of a four-button mechanical block and commercial Libera electronics [29]. This equipment provides beam position measurements at various data rates: the beam orbit is delivered at 10 Hz with submicrometer resolution, whereas the turn-by-turn data are sampled at the revolution frequency of 846.64 kHz with a 50-μm rms resolution, at 15 mA in the one quarter beam filling mode. This standard electronics was used to measure the betatron trajectory of the injected beam during the first turn.

However, in the case of the stored beam-based measurements, a greater resolution was required. In this perspective, the improved Libera Brilliance Plus electronics [31] has been commissioned and connected to a few BPMs. With these electronics, the turn-by-turn position resolution is reduced to 5 μm rms, at 15 mA in one quarter. Besides, the smearing effect between the turns introduced by the usual signal processing is avoided.

All the BPMs (and BLMs) acquisitions are synchronous and can be triggered on the injection event.

2. Beam size monitors

Two kinds of diagnostics are implemented in the SOLEIL storage ring to measure the transverse beam sizes. Both use the synchrotron radiation (SR) of one of the ring dipoles and source point imaging to infer the beam sizes. Of the first kind, the pinhole cameras use SR in the x-ray range and enable to achieve less than 10-μm-rms resolution. However, the minimum exposure time is in the tens of millisecond range, preventing fast measurements. The second kind uses SR in the visible range. Using a standard CMOS camera, the exposure time can be reduced to 30 μs. Using an ultra-fast KALYPSO camera, the exposure time can be further reduced to a few tens of nanoseconds, while the acquisition rate can reach 2.7 MHz [30], enabling to follow the beam size variations on a turn-by-turn basis. During the commissioning of the MIK, the variations of the transverse beam sizes have been characterized thanks to the KALYPSO camera. Since it is a linear camera, cylindrical lenses were used to match the radiation into the sensor. Horizontal and vertical beam size measurements were achieved successively, rotating the SR with a crossed polarizer. We tested several filling patterns (two-quarter filling pattern at 200 mA, one quarter filling pattern at 50 mA and 100 mA) in order to determine the most efficient setup for KALYPSO. The measurements showed that the minimum average current intensity necessary to produce a sufficient photon flux on the sensor equals 100 mA.

3. Beam loss monitors

The SOLEIL storage ring has been equipped with 80 BLMs since the end of 2020 that continuously detect and record the electron losses during machine operation. Those detectors were developed by the ESRF and are made of a scintillator (plastic rod, 22-mm diameter and 100 mm high) associated with a fast photomultiplier [32]. The detectors are installed perpendicular to the beam plane, which intersects the detectors at mid-height, at approximately 30 cm from the vacuum chamber on the internal side of the storage ring [33,34]. They are equally distributed all along the circumference, except for the injection and MIK sections which are over-equipped, and can detect the losses almost regardless of the direction of the particle showers thanks to their cylinder shape.

Dedicated fast electronics acquire and process the data. With a 6-ns temporal resolution, this system can provide turn-by-turn loss measurements and has been used to record and compare loss distributions associated to the standard and MIK injection scheme.

B. Diagnostics of the MIK section

The MIK is installed in a short straight section equipped with two standard BPMs installed, respectively, at the entrance and at the end of the section, similarly to all the other straight sections of the storage ring. The first BPM is 2.02 m upstream the entrance of the MIK, whereas the second one is 0.55 m downstream the end of the MIK. These BPMs are used to adjust the position of the stored beam in the MIK thanks to local bumps performed with the horizontal and vertical correctors surrounding the MIK section. In the case of typical horizontal bump of −200 μm in the MIK section, the peak value of the resulting beta beating is lower than 0.8% and the betatron tunes are shifted by -0.4×10^{-3}. The quadrupole feed-down experienced by the stored beam passing through sextupoles encompassed in the bump is not taken into account and we do not apply any kind of correction when performing bumps. Additionally, they are used to check if the injected beam passes through the MIK at the target position.

Apart from which, two BLMs are installed, respectively, aside of the first taper-absorber of the MIK and at the end of the straight section, as beam losses are distributed along this section (see Fig. 7).

Eventually, a set of thermocouples monitors the temperature of the flanges and the vacuum chamber of the MIK. All these diagnostics were valuable tools without which we could not have gone this far in the adjustment of the MIK injection.

VI. COMMISSIONING OF THE MIK

The complete MIK system was installed in the storage ring in January 2021. Preliminary experiments based on the stored beam validated several crucial steps such as the correct alignment of the MIK chamber, the correct field shape, and its linear variation with respect to the supplied current. The performance of the MIK has then been characterized.

A. Residual effects on the stored beam

The residual effects of the kickers and MIK on the stored beam have been characterized individually, while the septum magnets were turned off.

1. Turn-by-turn beam positions

In the following, Figs. 11–13 illustrate turn-by-turn data recorded thanks to the Libera Brilliance Plus electronics. The measurements are performed on a 15-mA beam, with only the second quarter of the ring fully filled with 104 bunches. This filling pattern was only used during the dedicated MIK experiments and was not considered as a limitation for turn-by-turn measurements of the beam position. Injection is inhibited and only the MIK or kickers are triggered, as if we were injecting in the second quarter. The horizontal and vertical chromaticities were minimized to 0.6 and 0.8, respectively, during the experiments in order to avoid beam decoherence and the bunch-by-bunch transverse feedback was switched off.

As shown in Fig. 11, the horizontal oscillation amplitude of the stored beam, due to the four kickers, equals approximately 350 μm whereas it is on the order of the micrometer using the MIK, i.e., below the rms resolution threshold of the Libera Brilliance Plus. To reach this level of stability, the stored beam was horizontally centered in the MIK by $\Delta x = -200$ μm. In this configuration, the stored beam is perfectly aligned with the magnetic center of the MIK. We see in Fig. 12 that the vertical oscillation amplitude induced by the four kickers equals almost 120 μm peak during the kicker pulse before stabilizing at roughly 60 μm peak. In the case of the MIK, the vertical perturbation is a bit weaker, since the oscillation amplitude equals approximately 40 μm peak, but without the initial transient.

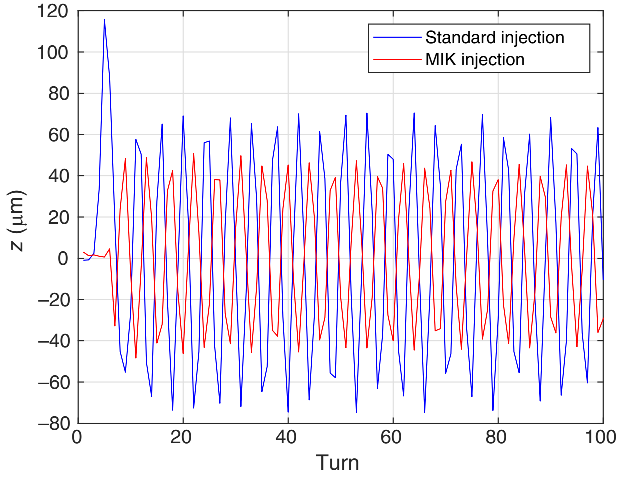

FIG. 12. Residual vertical betatron oscillations due to the four kickers (blue) and the MIK (red). Measurements with $\beta_z = 8.6$ m.

This vertical oscillation is out of tolerance, reaching 182% of the rms vertical stored beam size and could not be further minimized by means of horizontal, vertical bumps, or combination of both like it has been done to align the beam horizontally. This indicates the presence of a vertical dipolar defect, which had already been suspected by the magnetic measurements. Additional AT tracking studies pointed out oscillations identical to those measured by including a 5.4-μrad dipolar kick at the MIK location, which is finally in good agreement with the magnetic probe measurements.

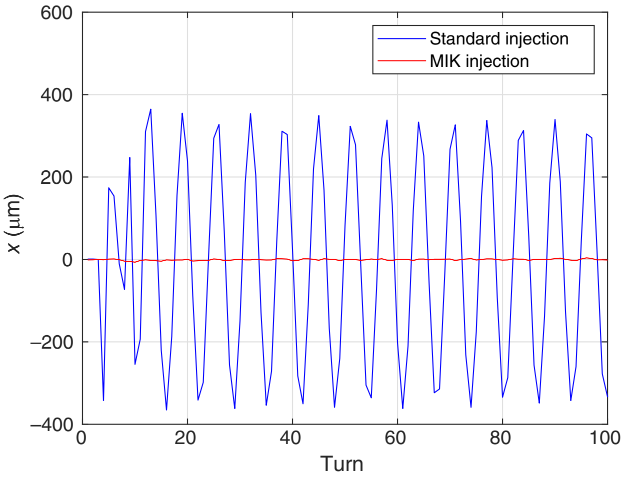

FIG. 11. Residual horizontal betatron oscillations due to the four kickers (blue) and the MIK (red). Measurements with $\beta_x = 13.3$ m.

The magnetic probe being in the clear, design studies of the MIK were conducted and provided enlightening results. First, the effects of Ti coating defects were simulated. As a result, it can be stated that the thickness of the left and right

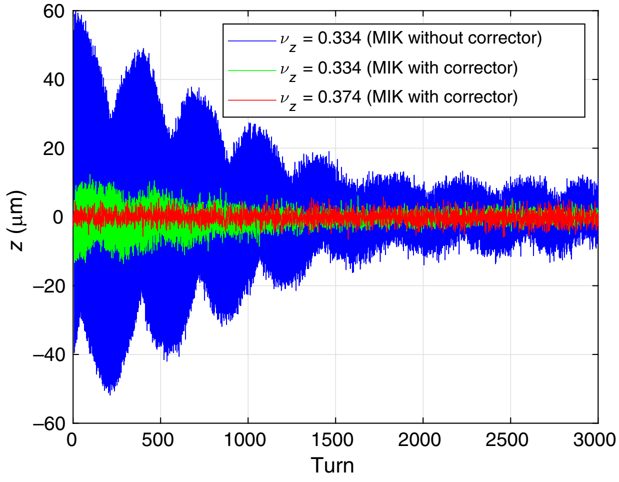

FIG. 13. Turn-by-turn variations of the vertical position of the stored beam. Measurements with $\beta_z = 12.1$ m. The MIK perturbs the beam which exhibits large betatron oscillations without correction, for $\nu_z = 0.334$ (blue). When the corrector is switched on, the amplitude of the betatron oscillations is divided by a factor of 6 (green). The correction is perfect for $\nu_z = 0.374$ (red).

side of the coating, whether it be symmetrical or not, has negligible effects on the central region of B_x compared to asymmetry between the upper and lower layer. In the latter case, the Eddy currents could induce a vertical dipolar defect in the field-free region. However, the asymmetry should be very significant, which is not the most probable scenario, as the temperature measured on the upper and lower part of the MIK chamber is the same. Eventually, the explanation can come from the cumulative misalignment errors of the eight conductors, due to the machined tolerances and the thickness of the epoxy glue. Indeed, the alignment tolerances of the conductors are very stringent: the positioning tolerances equal ±10 μm both horizontally and vertically, while the straightness tolerance equals ±10 μrad. A cumulative error of a few micrometers can lead to field defects whose order of magnitude is very similar to that measured. As an example, a cumulative misalignment of 25 μm transposed to the fourth conductor remarkably reproduces the measured dipolar defect in the field-free region of B_x, without affecting B_z.

Fortunately, a solution was found to completely compensate for this defect. Indeed, an active correction was tested successfully thanks to the reproducibility of the MIK. The compensation implements a pulsed vertical corrector located in the injection section. A dedicated pulser was fabricated in house to generate a pulse with one turn duration and a plateau lasting 300 ns, equivalent to the duration of a train of 104 bunches. The pulser was designed to provide a vertical kick in the 2 to 12 μrad range, which is needed to compensate for the vertical perturbation. Preliminary tracking simulations were carried out in order to determine the proper vertical phase advance between the MIK and the corrector, because it was verified that the default phase advance was not compatible with perfect correction, regardless of the corrector strength. Thus, the vertical tune was adjusted such that the vertical position of the beam at the corrector location was equal to zero, on the turn following the MIK kick. Then, the convenient magnitude of the kick has been determined, similarly to what had been done to minimize the Courant-Snyder invariant with the MIK. In the end, the corrector had to provide a 4-μrad vertical kick, after the kick of the MIK, in the case of $\nu_z = 0.374$ for the perturbation to vanish. The feasibility of the correction was demonstrated experimentally as the optimization of the correction with respect to the vertical tune is illustrated in Fig. 13.

In addition to the perfect compensation of the perturbation, this configuration also leaves the injection efficiency unchanged, measured at 85%.

Eventually, the MIK injection is set up such that the perturbation of the stored beam is below the rms resolution of 5 μm of the Libera Brilliance Plus electronics, in the horizontal and vertical plane. Furthermore, the benefits of the active correction was also confirmed thanks to the ultrafast KALYPSO camera.

2. Turn-by-turn beam size

The turn-by-turn measurement of the transverse stored beam sizes required a current intensity up to approximately 100 mA, as determined during the commissioning of KALYPSO (see Sec. V A 2). At such a current intensity, 104 bunches are required at least to avoid beam instabilities due to the charge per bunch and the bunch-by-bunch transverse feedback is necessarily switched on to avoid beam blowup. Again, only the second quarter is fully filled with 104 bunches, in order for the quadrupolar kick of the MIK to be as uniform as possible over the bunch train, limiting averaging effects, while providing enough photon flux for the detector. Similar to turn-by-turn position measurements, the horizontal and vertical chromaticities were adjusted to 0.6 and 0.8, respectively. Injection is inhibited and the MIK or the kickers are the only injection devices triggered. As previously mentioned, this measurement is performed in only one plane at a time (see Sec. V A 2). Typical KALYPSO images are illustrated in Fig. 14, gathering records in both planes while injecting with both magnets. For a given image, each vertical line corresponds to the beam transverse distribution in one plane at a given turn. The centroid of the beam corresponds to the peak intensity location along each vertical line. Thanks to the ultrafast acquisition rate of the camera, it is possible to follow the turn-by-turn evolution of the beam transverse profile, i.e. position and size, along the image's horizontal axis. The triggering of the injection is depicted by the vertical dotted white line on each image.

The measurements are processed to provide the variations of the rms transverse size of the stored beam and the position of its centroid with a precision on the order of a micrometer. The nominal beta functions, at the camera

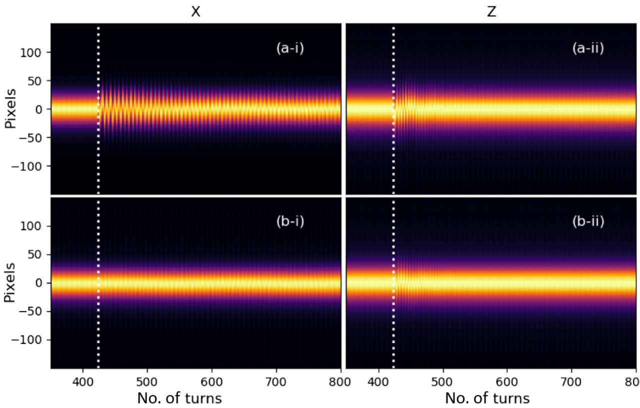

FIG. 14. Typical turn-by-turn imaging of the stored beam with the KALYPSO camera. The vertical white dotted line identifies the trigger of the injection devices and the beginning of the residual oscillations. (a-i) and (a-ii) are related to the kickers in the horizontal and vertical planes, respectively. (b-i) and (b-ii) are related to the MIK in the horizontal and vertical planes, respectively. The active correction is off.

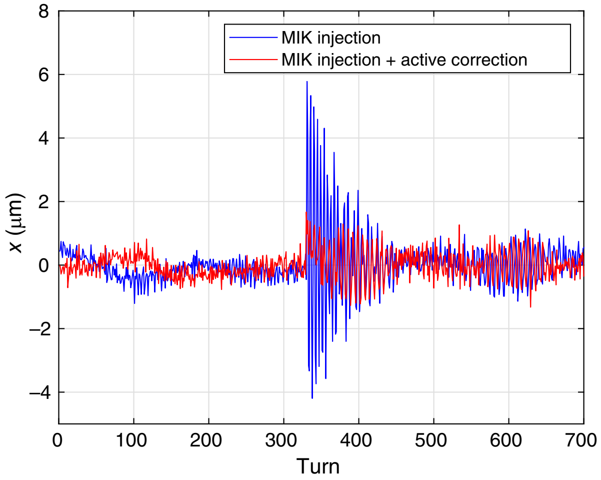

FIG. 15. Variations of the horizontal position of the stored beam due to a single triggering of the MIK, when the active correction is off (blue) and on (red). The slow varying modulation corresponds to synchrotron oscillations. This figure illustrates two processed KALYPSO images.

source point, are $\beta_x = 1.3$ m and $\beta_z = 11.4$ m, while $\beta_x = 1.5$ m and $\beta_z = 10.4$ m when $\nu_z = 10.374$. Figures 15 and 16 illustrate, respectively, the turn-by-turn variations of the horizontal and vertical position of the beam. At 100 mA, it is possible to measure residual betatron oscillations lower than 5 µm in the horizontal plane with KALYPSO, when the vertical corrector is turned off. The slow varying modulation illustrated in Fig. 15 corresponds to synchrotron oscillations. Of course, the vertical perturbation is also detected in the absence of active correction. It is worth noticing that the bunch-by-bunch transverse feedback does not decrease the peak value of the perturbation but rather decreases the damping time. As soon as the corrector is switched on, the perturbation vanishes in the vertical plane. It also has a positive effect on the horizontal betatron oscillations as the peak amplitude decreases from 5 µm to approximately 1 µm. This is due to the tiny uncorrected rolling angle of the corrector, confirmed thanks to beam-based measurements during its commissioning. As expected, since the corrector has a dipolar field, it has no benefit concerning the weak perturbation of the horizontal beam size.

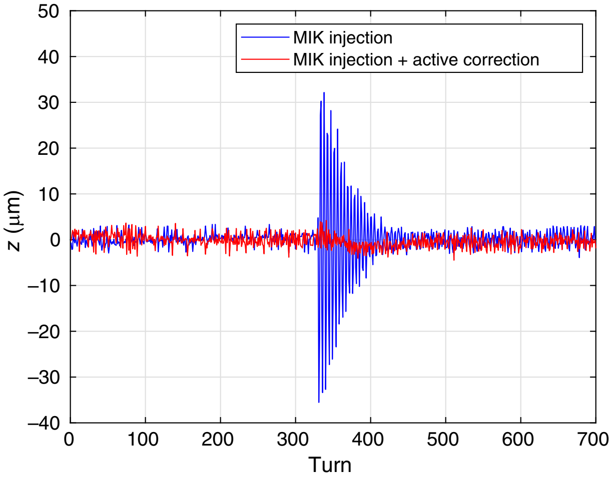

FIG. 16. Variations of the vertical position of the stored beam due to a single triggering of the MIK, when the active correction is off (blue) and on (red). This figure illustrates two processed KALYPSO images.

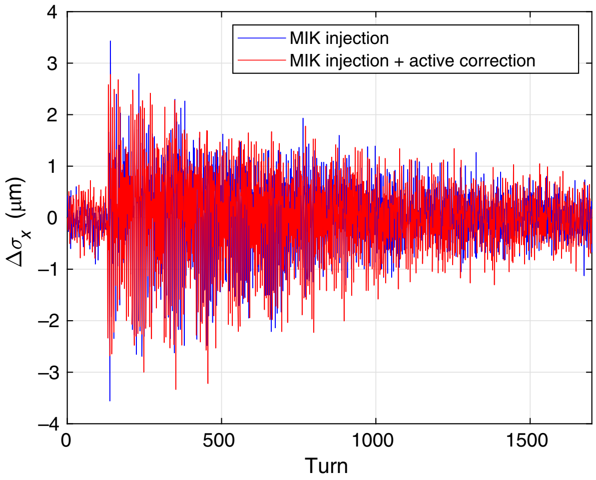

FIG. 17. Variations of the rms horizontal stored beam size due to the MIK. The peak variation is 3.5% of the rms horizontal stored beam size.

Horizontal beam size variations reaching a peak amplitude of approximately 3 µm are observed, as illustrated in Fig. 17. This represents 3.5% of the rms horizontal size of the beam. The bunch-by-bunch transverse feedback neither affects the amplitude of the perturbation nor its damping time because it implements a dipolar correction. On the other hand, the measurements in the vertical plane do not show any perturbation of the vertical size of the beam. This is expected since B_x does not have any transient quadrupolar component contrary to B_z.

These observations, which were never possible before, pave the way to further experiments. The ultimate goal is to characterize the level of transparency provided by the MIK injection to the users. In this perspective, injection tests are scheduled in a near future with three kinds of beamline at SOLEIL working in the infrared, soft x-ray, and hard x-ray ranges.

Not only the MIK appears as a major breakthrough in terms of stored beam stability but it also proved it is a reliable device on the injection end, as presented in the next section.

B. On-momentum betatron injection performance

We rapidly injected, stored, and accumulated electrons for the first time using the MIK, with an injection efficiency of roughly 40%. To increase the injection efficiency, the

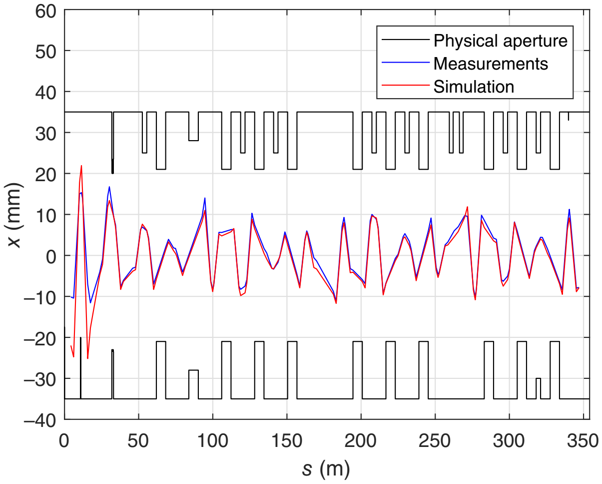

FIG. 18. Measured (blue) and simulated (red) horizontal first turn orbit. The horizontal physical aperture is plotted in black solid lines.

injected beam was steered horizontally and vertically at the injection point such that it could reach the target position in the MIK. In addition, the voltage of the MIK was set to 10 kV to provide a nominal kick of approximately 2 mrad. These optimizations brought the injection efficiency to a maximum of 97%. As foreseen by the simulations, the injected beam oscillates with a horizontal amplitude of approximately 25 mm until the MIK minimizes it to roughly 10 mm. This is illustrated in Fig. 18. It should be noted that the BPM response is considered non-linear beyond ±2 mm from the longitudinal axis of the storage ring. Consequently, for large oscillations of the beam, the data were processed to restore the real orbit [35]. However, the rebuilding algorithm does not converge as soon as the amplitude is equal to or greater than 25 mm, which explains the discrepancies between the measured and simulated positions between the injection point and the MIK.

After the commissioning of the superbend, the maximum injection efficiency measured in the bare lattice dropped to approximately 85% (see Sec. II B). However, fine-tuning the injection setup, in addition to non-linear optimization, will restore the performance in the near future, at least partially. Whether it be before or after the installation of the superbend, injection is more efficient using the MIK because the minimum dynamic aperture needed is narrower compared to that needed for the standard injection scheme.

Although the BLMs do not distinguish the vertical losses from the horizontal ones, the AT model predicts that most of the injection losses happen in the vertical plane through nonlinear coupling. Figures. 19 and 20 illustrate the turn-by-turn injection losses along the storage ring, in the case of the standard and MIK injection, respectively. The majority of the injection losses are detected in a few medium straight sections with tight physical apertures of ±5 mm vertically and ±21 mm horizontally. Besides, the superbend vacuum chamber has a minimum vertical aperture of ±6 mm which also intercepts some electrons. The rest of the injection losses are detected in the injection and MIK sections. The injection losses associated with the kicker injection scheme happen periodically during the first 4000 turns with the synchrotron period (Fig. 19), whereas it is negligible after approximately the turn 3500 in the case of the MIK (Fig. 20). In both cases, after turn 4000, most of the losses are detected in the first quarter of the storage ring.

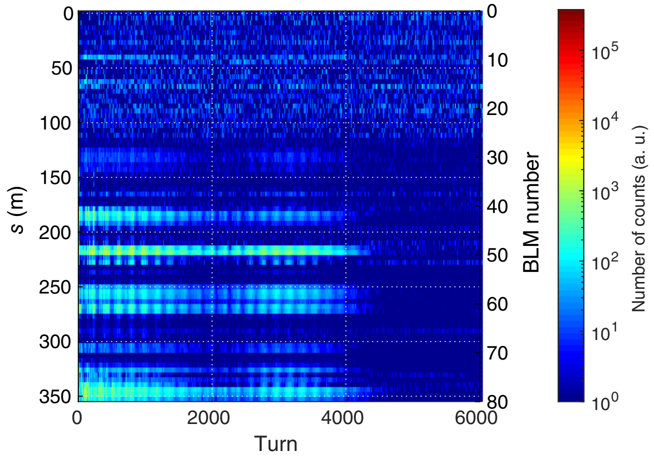

FIG. 19. Turn-by-turn losses distribution in the case of the standard injection scheme. BLMs 1 to 25 monitor the beam losses from the injection to the MIK sections.

Besides, based on decay loss measurements, it is necessary to insert the inner horizontal scraper at −20 mm, instead of the previous nominal position of −28 mm, to protect the MIK. The new position of the blade does not completely shield the MIK but provides sufficient protection while maintaining an injection efficiency and a beam lifetime compatible with the operation. In operation, the major part of the injection and decay

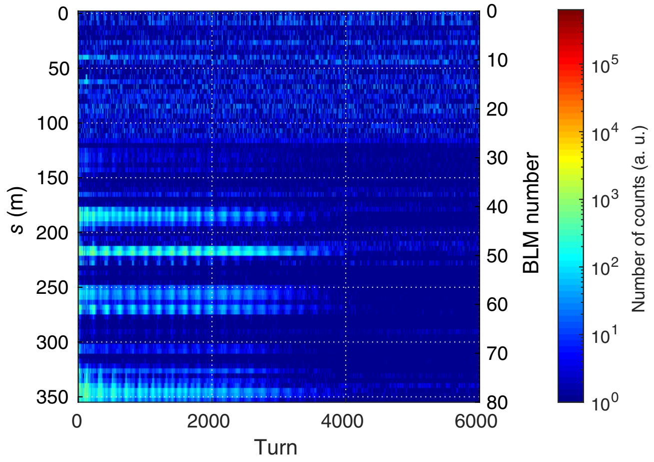

FIG. 20. Turn-by-turn losses distribution in the case of the MIK injection scheme. BLMs 1 to 25 monitor the beam losses from the injection to the MIK sections.

losses can be relocated in the injection section as soon as the vertical scrapers are additionally inserted to their nominal value of ± 3 mm.

Finally, we report in the next section useful observations about the moderate heating of the MIK chamber by the circulating beam in various filling patterns.

C. Heating concerns

The very first beam current ramp of the storage ring up to its nominal stored current of 500 mA after the installation of the MIK revealed a major and unexpected heating of its chamber. The temperature reached 130 °C on its downstream end at only 300 mA. Our initial air-cooling system turned out to be not efficient enough. Thus, the heat dissipation and airflow were improved around the chamber by adding extra heavy-duty forced air turbines. This currently provides a manageable temperature rise while reaching the nominal current of all the operation modes. Still, using this setup, a significant temperature imbalance was found between the upstream and downstream ends of the MIK. Later on, dedicated machine studies further concluded the heat load was not linearly dependent on stored current, ruling out synchrotron radiation as a contributor to this unexpected heating.

The postinstallation investigations and thermal simulations confirmed the initial estimate of the maximum heat load of 156 W. The corresponding power density of $3.6\ \mathrm{W\,mm^{-2}}$ was in agreement with the temperatures measured on the upstream end, both with and without the additional fans. Thermal simulations implementing finite element analysis (FEA) were used to describe the thermal behavior of the magnet and to determine the origin of the heating. A local degradation of the Ti coating or a partial loss of the rf contact with the neighboring flange could explain the anomalous heating on the downstream end of the MIK. The heat load distribution in the Ti coating was calculated in each filling mode case. This takes the actual measured resistivity and thickness of the Ti coating into account. The heat loads due to small varying apertures at the rf contact in the flanges were also calculated by FEA and used in the thermal model.

The simulated nominal operation case, corresponding to a 500 mA uniform filling, including three forced air cooling turbines, shows good agreement with measurements on the upstream end of the chamber (see Table VI). The temperature of the actual MIK chamber is measured with several sensors and ranges between 86 and 125 °C at the downstream end. The simulation of a complete electrical discontinuity in the downstream flange shows unreasonable discrepancies with the measurements compared to the case of a perfect electrical contact. Besides, the temperature measurements indicate that the hot spot is most likely to be located in the MIK rather than in the flange. Thus, one possible scenario is that the heat spread to the downstream flange due to small defects in the Ti coating responsible for the temperature rise. In this context, an imperfect rf contact might also be an additional factor. The impedance and thermal studies are detailed in [36].

TABLE VI. Measured and simulated temperatures of the MIK chamber, at 500 mA, including forced air cooling.

	Measured	Simulated
Upstream temperature (°C)	52 to 63	60
Downstream temperature (°C) continuous/discontinuous rf contact	86 to 125	60/···

A full disassembly of the MIK and flanges is planned to visually inspect the Ti coating and the quality of the electrical contacts between the flanges and the various parts. Certainly, the Ti coating is one of the crucial aspects of the MIK design and requires special attention. It already required the removal of the very first MIK commissioned at MAX IV in 2017 because of heating issues due to a too-thin layer of titanium [8,24].

Currently, the 110 mA eight-bunch filling pattern leads to the highest temperatures, in the range of 70 and 160 °C, respectively at the upstream and downstream ends of the MIK chamber, which was deemed acceptable for the continuous operation. Additional machine interlocks were implemented to protect the MIK chamber in case of failure of one of the turbines.

VII. CONCLUSION

In the wake of the global effort to achieve transparent injection over the past decade, an MIK was successfully commissioned at SOLEIL in 2021. It is the third time that a SOLEIL-built MIK is commissioned, one of them is currently used for daily operation in the MAX IV diffraction limited storage ring.

At SOLEIL, the MIK proved it can be the milestone of an innovative off-axis injection scheme compatible with the operation. Indeed, the careful setup of the MIK injection enabled it to reach a peak injection efficiency of 97% in the bare lattice during summer 2021, slightly better than that of the standard bump-based scheme. This advantage was confirmed even after the installation of the permanent magnet–based 2.8-T superbend.

The experimental and simulation studies to understand the unexpected early temperature rise of the MIK are well advanced and provide precious insights into the key points to master during its conception and assembly steps. The cooling system was underestimated. In particular, the titanium has to be uniformly coated inside the vacuum chamber of the MIK. The thickness of 3.5 μm is an optimal balance between heat load and Eddy current–induced transient quadrupolar fields.

In terms of stored beam perturbations, the MIK outperforms the four kickers. In the horizontal plane, the residual perturbation is divided by almost a factor of 100. It is on the order of a few micrometers without additional active correction, below 2% of the rms size of the stored beam. Moreover, the residual vertical perturbation, specific to the MIK of SOLEIL, was completely compensated thanks to a new working point configuration and a vertical corrector. Not only did this compensation preserve the maximum injection efficiency achievable but it also enhanced the stored beam stability in the horizontal plane, as confirmed by the measurements performed with the ultrafast camera KALYPSO. This defect highlights the challenges inherent to stringent positioning tolerances of the conductors (±10 μm with ±10-μrad straightness). A new pulser may be developed in order to provide a larger corrector pulse and consequently extend this correction to the four-quarters of the beam in the 500-mA filling mode.

In addition, the variations of the rms horizontal size of the stored beam are held in the 3-μm range in the horizontal plane, i.e., 3.5% of the rms horizontal stored beam size. Incidentally, preliminary experimental studies conducted with an infrared beamline of SOLEIL revealed the first improvements in terms of injection transparency. These will lead to complementary in-depth studies during summer 2022 to be conducted with other beamlines very sensitive to injection-induced distortions. All these achievements invite further injection experiments, such as off-momentum and longitudinal MIK injections, that will provide enlightening information for the future injection scheme of the SOLEIL Upgrade project.

ACKNOWLEDGMENTS

We would like to deeply thank the Accelerator Physics, Diagnostics, Power Supply, and Pulsed Magnet Groups of SOLEIL for many insightful discussions. We are grateful to Amor Nadji, head of the Engineering and Accelerators Division of SOLEIL, A. Loulergue, for many discussions in the early phase of the project and the measurements to characterize the four-kicker injection and the booster, R. Broucquart (Diagnostics) and J.-B. Pruvost (Radiation Safety) and the Operation Group. Finally, the whole MIK project team is warmly thanked. This work is partly realized in the framework of the first author's Ph.D. (Paris-Saclay University), headed by R. Nagaoka and co-supervised by L. S. Nadolski (Accelerator Physics).

---

[1] H. Tanaka, T. Ohshima, K. Soutome, and M. Takao, Suppression of injection bump leakage caused by sextupole magnets within a bump orbit, Nucl. Instrum. Methods Phys. Res., Sect. A **539**, 547 (2005).

[2] S. White, J. Chavanne, M. Dubrulle, G. Le Bec, E. Plouviez, P. Raimondi, and B. Roche, Damping of injection perturbations at the European Synchrotron Radiation Facility, Phys. Rev. Accel. Beams **22**, 032803 (2019).

[3] S. Leemann, Pulsed sextupole injection for Sweden's new light source MAX IV, Phys. Rev. ST Accel. Beams **15**, 050705 (2012).

[4] H. Takaki, N. Nakamura, Y. Kobayashi, K. Harada, T. Miyajima, A. Ueda, S. Nagahashi, M. Shimada, T. Obina, and T. Honda, Beam injection with a pulsed sextupole magnet in an electron storage ring, Phys. Rev. ST Accel. Beams **13**, 020705 (2010).

[5] O. Dressler, T. Atkinson, M. Dirsat, and P. Kuske, Development of a non-linear kicker system to facilitate a new injection scheme for the BESSY II storage ring, in Proceedings of 2nd International Particle Accelerator Conference, IPAC2011, San Sebastián, Spain (JACoW, Geneva, Switzerland, 2011)

[6] S. C. Leemann and L. O. Dallin, Progress on Pulsed Multipole Injection for the MAX IV Storage Rings, in *Proceedings of 2013 North American Particle Accelerator Conference, Pasadena, CA* (JACoW, Geneva, Switzerland, 2013), pp. 1052–1054.

[7] J. da Silva Castro, P. Alexandre, R. Ben El Fekih, and S. Thoraud, Multipole injection kicker (MIK), a cooperative project SOLEIL and MAX IV, in *Proceedings of 10th Mechanical Engineering Design of Synchrotron Radiation Equipment and Instrumentation (MEDSI'18), Paris, France, 2018* (JACoW, Geneva, Switzerland, 2018), pp. 48–49.

[8] P. Alexandre, R. Ben El Fekih, A. Letrésor, S. Thoraud, J. da Silva Castro, F. Bouvet, J. Breunlin, Å. Andersson, and P. Tavares, Transparent top-up injection into a fourth-generation storage ring, Nucl. Instrum. Methods Phys. Res., Sect. A **986**, 164739 (2021).

[9] R. Ollier, P. Alexandre, R. Ben El Fekih, and L. S. Nadolski, Design and commissioning of a multipole injection kicker for the SOLEIL storage ring, in *Proceedings of 12th International Particle Accelerator Conference, IPAC'21, Campinas, SP, Brazil* (JACoW, Geneva, Switzerland, 2021), pp. 3525–3528, 10.18429/JACoW-IPAC2021-WEPAB353.

[10] A. Nadji, Synchrotron SOLEIL upgrade project, in *Proceedings of 12th International Particle Accelerator Conference, IPAC'21, Campinas, SP, Brazil* (JACoW, Geneva, Switzerland, 2021), pp. 463–465, 10.18429/JACoW-IPAC2021-MOPAB131.

[11] Conceptual design report: Synchrotron SOLEIL upgrade, https://www.synchrotron-soleil.fr/en/news/conceptual-design-report-soleil-upgrade (2021).

[12] A. Loulergue, D. Amorim, P. Brunelle, A. Gamelin, A. Nadji, L. S. Nadolski, R. Nagaoka, R. Ollier, and M.-A. Tordeux, CDR baseline lattice for the upgrade of SOLEIL, in *Proceedings of 12th International Particle Accelerator Conference, IPAC'21, Campinas, SP, Brazil* (JACoW, Geneva, Switzerland, 2021), pp. 1485–1488.

[13] SOLEIL website, https://www.synchrotron-soleil.fr.

[14] L. S. Nadolski *et al.*, SOLEIL update status, in *Proceedings of 12th International Particle Accelerator Conference, IPAC'21, Campinas, SP, Brazil* (JACoW, Geneva, Switzerland, 2021), pp. 3945–3948, 10.18429/JACoW-IPAC2021-THPAB078.

[15] A. Nadji *et al.*, A modified lattice for SOLEIL with a larger number of straight sections, in *Proceedings of 5th*

Shanghai Symposium on Intermediate-energy Light Sources, SSILS2001, Shanghai, China, 2001 (2001).

[16] J. Laskar *et al.*, Introduction to frequency map analysis, in *Proceedings of 3DHAM95 NATO Advanced Institute, 1995* (1995), pp. 134–150, 10.1007/978-94-011-4673-9_13.

[17] M.-A. Tordeux, J. Da Silva Castro, P. Feret, P. Gros, P. Lebasque, and A. Mary, General performances of the injection scheme into the SOLEIL storage ring, in *Proceedings of the 9th European Particle Accelerator Conference, Lucerne, 2004* (EPS-AG, Lucerne, 2004), pp. 2044–2046.

[18] J. Kallestrup and M. Aiba, Emittance exchange in electron booster synchrotron by coupling resonance crossing, Phys. Rev. Accel. Beams **23**, 020701 (2020).

[19] P. Lebasque, R. Ben El Fekih, M. Bol, J.-P. Lavieville, A. Loulergue, and D. Muller, Improvement on pulsed magnetic systems at SOLEIL, in *Proceedings of the 11th European Particle Accelerator Conference, Genoa, 2008* (EPS-AG, Genoa, Italy, 2008), pp. 2183–2185.

[20] A. Loulergue, Residual orbit corrections for top-up at SOLEIL (2009), http://archive.synchrotron.org.au/%22images/proceedings/topup/ top-up10_loulergue.pdf/%22.

[21] P. Lebasque, Injection systems for 3rd generation light sources, https://indico.cern.ch/event/74380/contributions/2087131/attachments/1045487/1490183/Injection_systems_for_3rd_light_sources-V2.pdf (2010).

[22] A. Loulergue, Injection and top-up experience at SOLEIL, https://indico.cern.ch/event/635514/contributions/2660453/attachments/1518204/ (2017).

[23] The European Synchrotron Radiation Facility website, https://www.esrf.fr/.

[24] J. Kallestrup *et al.*, Studying the dynamic influence on the stored beam from a coating in a multipole injection kicker, in *Proceedings of 10th International Particle Accelerator Conference, IPAC'19, Melbourne, Australia, 2019* (JACoW, Geneva, Switzerland, 2019), pp. 1547–1550, 10.18429/JACoW-IPAC2019-TUPGW063.

[25] QuickField Professional v6.3.1.2049 by Tera Analysis Ltd, https://quickfield.com.

[26] Accelerator Toolbox Collaboration, https://github.com/atcollab/at.

[27] T. Heller, Toolkit for Simulated Commissioning (SC), https://sc.lbl.gov.

[28] J. Bengtsson, E. Forest, and H. Nishimura, TRACY III, then translated by M. Böge at SLS and extended by L. S. Nadolski at SOLEIL (2002) and revised by J. Bengtsson at BNL (2005). A compact user interface was added at SOLEIL by J. Zhang (2011).

[29] N. Hubert, L. Cassinari, J.-C. Denard, N. Leclercq, A. Nadji, L. N. Nadolski, and D. Pedeau, The SOLEIL BPM and orbit feedback systems, in *Proceedings of 8th European Workshop on Beam Diagnostics and Instrumentation for Particle Accelerators, DIPAC'07, Venice, Italy, 2007* (2007), pp. 189–191, https://accelconf.web.cern.ch/d07/papers/TUPC20.pdf.

[30] M. M. Patil *et al.*, Ultra-fast line-camera KALYPSO for fs-laser-based electron beam diagnostics, in *Proceedings of 10th International Beam Instrumentation Conference, IBIC'21, Online, Korea* (JACoW, Geneva, Switzerland, 2021), pp. 1–6, 10.18429/JACoW-IBIC2021-MOOB01.

[31] Instrumentation Technologies, https://www.i-tech.si/products/libera-brilliance-3/.

[32] P. Leban and K. B. Scheidt, Prototype results with a complete beam loss monitor system optimized for synchrotron light sources, in *Proceedings of 6th International Particle Accelerator Conference (IPAC'15), Richmond, VA, 2015* (JACoW, Geneva, Switzerland, 2015) pp. 1019–1021, 10.18429/JACoW-IPAC2015-MOPTY041.

[33] N. Hubert, M. E. Ajjouri, and D. Pédeau, Test of new beam loss monitors for SOLEIL, in *Proceedings of 7th International Beam Instrumentation Conference, IBIC'18, Shanghai, China, 2018* (JACoW, Geneva, Switzerland, 2019), pp. 215–218, 10.18429/JACoW-IBIC2018-TUPA03.

[34] N. Hubert, M. E. Ajjouri, and D. Pédeau, New beam loss monitor system at SOLEIL, in *Proceedings of 8th International Beam Instrumentation Conference, IBIC'19, Malmo, Sweden* (JACoW, Geneva, Switzerland, 2019), pp. 118–121, 10.18429/JACoW-IBIC2019-MOPP017.

[35] N. Hubert, B. Béranger, and L. S. Nadolski, BPM data correction at SOLEIL, in *Proceedings of 5th International Particle Accelerator Conference, IPAC'14, Dresden, Germany, 2014* (JACoW, Geneva, Switzerland, 2014), pp. 3430–3432 10.18429/JACoW-IPAC2014-THPME083.

[36] A. Gamelin *et al.*, Investigation of RF heating for the multipole injection kicker installed at SOLEIL, in *Proceedings of 13th International Particle Accelerator Conference, IPAC'22, Bangkok, Thailand* (JACoW, Geneva, Switzerland, 2022).